

# DSCA: A Digital Subtraction Angiography Sequence Dataset and Spatio-Temporal Model for Cerebral Artery Segmentation

Qihang Xie, Mengguo Guo, Lei Mou, Dan Zhang, Da Chen, Caifeng Shan,  
Yitian Zhao, Ruisheng Su, and Jiong Zhang

**Abstract**—Cerebrovascular diseases (CVDs) remain a leading cause of global disability and mortality. Digital Subtraction Angiography (DSA) sequences, recognized as the golden standard for diagnosing CVDs, can clearly visualize the dynamic flow and reveal pathological conditions within the cerebrovasculature. Therefore, precise segmentation of cerebral arteries (CAs) and classification between their main trunks and branches are crucial for physicians to accurately quantify diseases. However, achieving accurate CA segmentation in DSA sequences remains a challenging task due to small vessels with low contrast, and ambiguity between vessels and residual skull structures. Moreover, the lack of publicly available datasets limits exploration in the field. In this paper, we introduce a DSA Sequence-based Cerebral Artery Segmentation Dataset (DSCA), the first publicly accessible dataset designed specifically for pixel-level semantic segmentation of CAs. Additionally, we propose DSANet, a spatio-temporal network for CA segmentation in DSA sequences. Unlike existing DSA segmentation methods that focus only on a single frame, the proposed DSANet introduces a separate temporal encoding branch to capture dynamic vessel details across multiple frames. To enhance small vessel segmentation and improve vessel connectivity, we design a novel TemporalFormer module to capture global context and correlations among sequential frames. Furthermore, we develop a Spatio-Temporal Fusion (STF) module to effectively integrate spatial and temporal features from the encoder. Extensive experiments demonstrate that DSANet outperforms other state-of-the-art methods in CA segmentation, achieving a Dice of 0.9033.

**Index Terms**—DSA, cerebrovascular disease, cerebral artery segmentation, spatio-temporal fusion.

## I. INTRODUCTION

Cerebrovascular diseases (CVDs) are significant causes of death, resulting in considerable suffering for patients and plac-

ing substantial financial pressure on families [1]. The majority of CVDs, such as stroke, moyamoya disease, and cerebral aneurysms, affect the geometrical and topological conditions of cerebral arteries (CAs). Therefore, analyzing CAs by segmenting and classifying them into bifurcated vessels (BV) and the main artery trunk (MTA) is essential for revealing vascular abnormalities associated with these diseases, leading to timely diagnosis and treatment planning [2].

In clinical practice, several imaging techniques such as computed tomography angiography (CTA), magnetic resonance angiography (MRA), and digital subtraction angiography (DSA) are commonly used for the diagnosis and treatment of CVDs. Among them, DSA offers dynamic imaging of cerebral vessels with high spatial and temporal resolution, providing accurate details of lesions [3]. It is thus commonly used as the golden standard for diagnosing CVDs by clinicians, in cases where CTA and MRA fail to provide accurate diagnosis. However, the examination using DSA heavily relies on visual inspection by radiologists, which can be time-consuming and labor-intensive. Furthermore, radiologists with limited experience may be susceptible to misdiagnosis and underdiagnosis. Therefore, automated segmentation of CAs in DSA sequences, with the capability of capturing precise cerebrovascular details, offers valuable features to expedite the diagnosis and treatment.

In terms of vascular segmentation, geometric-based and learning-based techniques have experienced rapid development and shown considerable promise in different modalities. Compared to traditional methods such as model-based [4] and tracking-based methods [5], deep learning-based techniques demonstrate superior robustness in cerebrovascular segmentation [6], [7]. Notably, the UNet architecture [8] emerges as an important milestone, with its diverse variants being widely adopted for both 2D and 3D segmentation tasks [9]–[11]. These models incorporate carefully designed components, such as improved skip connections [7], [12], [13], multi-scale module designs [7], [14], [15], attention mechanisms [16]–[18], and transformer blocks [19]–[21], aiming at augmenting segmentation efficacy. Besides that, certain studies explore aspects beyond network structure considerations. For instance, Isensee *et al.* [22] introduced nnUNet, a UNet model incorporated with extensive data preprocessing and training strategies, which proved successful in numerous segmentation competitions. Zhang *et al.* [23] improved coronary artery segmentation by utilizing a multi-task approach that prioritized center-

Q. Xie, L. Mou, Y. Zhao, and J. Zhang are with the Laboratory of Advanced Theranostic Materials and Technology, Ningbo Institute of Materials Technology and Engineering, Chinese Academy of Sciences, Ningbo 315201, China.

Q. Xie is also with the Cixi Biomedical Research Institute, Wenzhou Medical University, Ningbo, China.

M. Guo is with the First Affiliated Hospital of Zhengzhou University, Zhengzhou, China.

D. Zhang is with the School of Cyber Science and Engineering, Ningbo University of Technology, Ningbo, China.

D. Chen is with the Qilu University of Technology, Jinan, China.

C. Shan is with the School of Intelligence Science and Technology, Nanjing University, Nanjing, China.

R. Su is with the Erasmus MC, University Medical Center, Rotterdam, Netherlands. He is also with the Department of Biomedical Engineering, Eindhoven University of Technology, Eindhoven, Netherlands.

J. Zhang is also with the Laboratory of Neuro Imaging (LONI), Keck School of Medicine of University of Southern California, Los Angeles, CA 90033, United States. Corresponding author: jiong.zhang@ieee.org

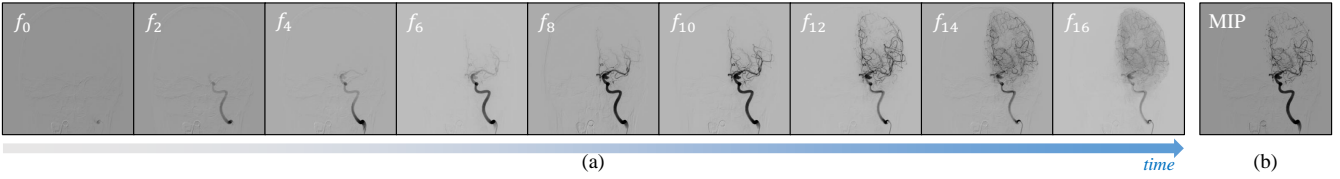


Fig. 1. (a) is a DSA sequence, which includes 17 frames in the arterial phase. (b) is the MIP image of the arterial phase of the DSA sequence.

line segmentation. In the field of cerebrovascular segmentation, some researchers explored the integration of Generative Adversarial Networks (GANs) to improve the segmentation performance [6], while others leverage semi-supervised and unsupervised methodologies to address challenges associated with data labeling [24], [25].

Nevertheless, there is limited research on CA segmentation in DSA images. Zhang *et al.* [26] first proposed a straightforward U-shaped network for single-frame segmentation of DSA cerebral vessels. Meng *et al.* [7] introduced the MDCNN framework, leveraging CNN with multi-scale dense connections in conjunction with an entropy-sampled patch method for single-frame DSA segmentation. Xu *et al.* [27] proposed an edge regularization network (ERNet) for segmenting vessels in DSA images. ERNet uses erosion and dilation on the initial binary annotations to create pseudo-ground-truths for false negative and false positive cases. Subsequently, Vepa *et al.* [28] proposed a weakly supervised approach employing an active contour model to generate pseudo-labels for DSA vessel segmentation. However, despite these advancements, the segmentation performance of these methods still suffers from the low contrast of small vessels, and the interference from residual skull structures. Additionally, these methods focus only on pixel-by-pixel vessel extraction, while further classifying the vessel into bifurcated vessels (BV) and main artery trunk (MTA) is more clinically significant, e.g., for automatic detection and evaluation of stenosis, and automatic scoring for thrombolysis of cerebral infarction [29]. Moreover, regardless of whether fully supervised or weakly supervised methods are employed, existing approaches typically confine training on a single frame extracted from DSA sequences, leading to unstable microvascular segmentations.

In clinical practice, a DSA sequence displays dynamic flows of vessels, where each frame captures only a fraction of the contrast agent, as depicted in Fig. 1-(a). Moreover, pathological changes such as arterial stenosis, collateralization, and aneurysms associated with various diseases exhibit significant variability across DSA sequences, appearing at uncertain frames within the sequence and manifesting diverse morphological characteristics. Consequently, relying solely on a single DSA frame for segmentation fails to cover the entire cerebrovasculature and these pathological features adequately. Unfortunately, a publicly available dataset that comprehensively labels entire dynamic blood flows is currently absent, primarily due to the labor-intensive nature of annotating such a sequence compared to labeling an individual frame. As illustrated in Fig. 1, the minimum intensity projection (MIP) image reveals the complete angiogram, incorporating infor-

mation from all frames. These observations motivate us to consider training on entire DSA sequences and performing labeling on the MIP image. This approach not only preserves the complete cerebrovascular features but also alleviates the annotation workload simultaneously.

Therefore, in this work, we establish a DSA Sequence dataset, comprising 224 DSA sequences of several common CVDs. To address the segmentation challenges, we propose a spatio-temporal network (DSANet) for CA segmentation. It takes a DSA sequence and its MIP image as input to produce a complete 2D segmentation. Unlike 2D segmentation methods that only use a spatial encoding branch (SEB), our network includes an independent temporal encoding branch (TEB) to capture crucial temporal information. Following the TEB, we treat each frame in the sequence as a token, leveraging TemporalFormer blocks to capture global flow information from the DSA sequence. Subsequently, the spatial and temporal features from the two encoding branches are effectively fused through the spatio-temporal fusion (STF) module. In summary, our main contributions can be outlined as follows:

- We establish the first publicly accessible **DSA-Sequence based Cerebral Artery** segmentation dataset (DSCA), consisting of pixel-wise cerebrovascular annotations across 224 DSA sequences from several common CVDs. To promote further developments in this field, the DSCA dataset, the code, and baseline models are made available at this website.
- We propose a novel spatio-temporal strategy aimed at enhancing cerebral artery segmentation within DSA sequences. We design two encoding branches, i.e., the TEB and SEB, which respectively employ the sequence images and MIP images as input, to leverage both spatial and temporal information for precise segmentation of the entire cerebrovasculature.
- To improve segmentation connectivity, we propose treating each frame as individual tokens following the TEB. These tokens are combined and fed into specially designed TemporalFormer blocks to effectively capture global context and dynamic correlations among frames across the sequence.
- We introduce a new STF module to integrate spatial and temporal features from the encoders. This module effectively addresses ambiguity among BV, MTA, and residual skulls by leveraging the dynamic changes of vessels and the structural invariance of the skull.

## II. DATASET

### A. Dataset Description

The DSCA dataset was collected from intraoperative and postoperative DSA imaging at the First Affiliated Hospital of Zhengzhou University, Zhengzhou, China. The acquisition

TABLE I  
DATASET COMPARISON

Dataset	Sample	Resolution	Type	Public
Meng <i>et al.</i> [7]	30	700 × 700	Single Frame	No
Zhang <i>et al.</i> [26]	20	512 × 512	Single Frame	No
Vepa <i>et al.</i> [28]	128	1024 × 1024	Single Frame	No
Fu <i>et al.</i> [30]	88	1024 × 1024	Single Frame	No
Xu <i>et al.</i> [27]	138	800 × 800	Single Frame	No
<b>DSCA</b>	<b>224</b>	<b>Multiple</b>	<b>Sequence</b>	<b>Yes</b>

of these subjects was retrospectively between January 2022 and July 2023, with patient identifiers removed to protect privacy. All the data used in this study were collected under the approval of institutional ethics committees and consented by the participants, following the Declaration of Helsinki.

The DSCA dataset consists of 58 patients, in total 224 DSA sequences including 1792 images from the left and right hemispheres. Among them, there are 28 male and 30 female patients, with ages ranging from 9 to 81 years and an average age of 49. Notably, the DSA sequences include three different arteries: the internal carotid artery (ICA), external carotid artery (ECA), and vertebral artery (VA). Specifically, there are 126 sequences for ICA, 55 for ECA, and 43 for VA. These sequences were captured by multiple imaging devices including AXION-Artis-160145 and AXION-Artis-160480 (Siemens, Germany), Azurion-559, Azurion-703844, AlluraXper-722012-2542 and AlluraXper-722038-129 (Philips, Netherlands), and Bransist Safire VC17 (Shimadzu, Japan), with sampling rates ranging from 4 to 7 frames per second. Moreover, these sequences exhibit different resolutions (from  $512 \times 472$  to  $1432 \times 1432$ ). Each DSA sequence, captured in coronal or sagittal views, was stored in a DICOM file, with 108 DSA sequences in the coronal view and 116 in the sagittal view. All sequences retained arterial phase frames while discarding non-contrast, capillary phase, and venous phase frames [29], guided by the neurosurgeon’s expertise. Consequently, DSA sequences in the DSCA dataset consist of 5 to 22 frames. To align with network input, we resample all DSA sequences to 8 frames based on the distribution of extracted arterial phase frames. Detailed information about the dataset is provided in the GitHub.

### B. Manual Annotation Protocol

As mentioned above, manually annotating the complete DSA sequence is a time-consuming and labor-intensive task. In contrast, annotating the corresponding MIP image can save considerable time while retaining the entire cerebrovascular information. Furthermore, distinguishing between BV and MTA holds greater clinical significance. Thus, we asked skilled clinicians to manually annotate the MIP images, including specific labeling for both BV and MTA. These annotations served as the gold standard for the DSCA dataset. The data preprocessing and annotation procedures are as follows: (1) Selection of arterial phase frames from the DSA sequences. (2) Registration of the extracted arterial phase sequence frames using Elastix [31], followed by resampling to 8 frames. (3)

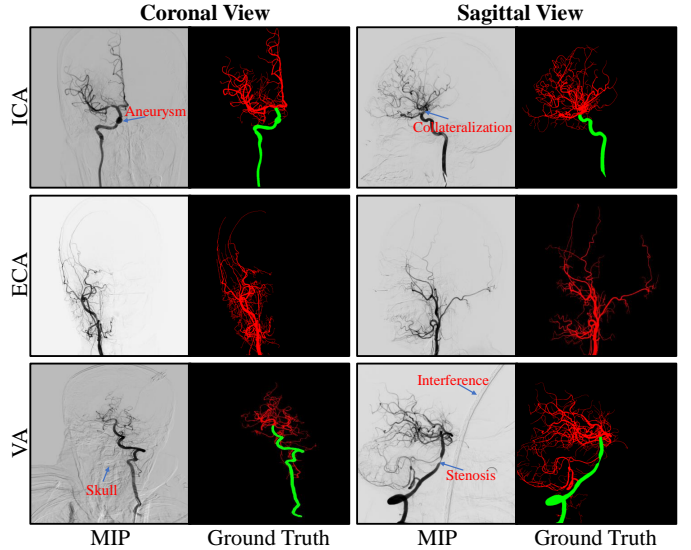


Fig. 2. The annotating examples of the DSCA dataset. The first to third rows are ICA, ECA, and VA. The 1st and 2nd column are coronal view, and the 3rd and 4th column are sagittal view.

Projection of the resampled frames to generate MIP images. (4) Annotation of the MIP images utilizing ITK-SNAP [32].

The annotation process of the DSCA dataset was performed by five skilled clinicians who received complete training. Disputed annotations were referred to a senior neurosurgeon for confirmation. Subsequently, a second senior neurosurgeon conducted a final review and revision of all annotations. The annotated results of the DSCA dataset are presented in Fig. 2, wherein the ICA and VA sequences were categorized into background, BV, and MTA. The ECA sequences, lacking a distinct main trunk, were classified into background and BV. To mitigate potential risks of data leakage, the DSA sequences were randomly divided based on patient IDs into a training set comprising 80% of the data and a test set comprising the remaining 20%. Consequently, the training set comprises 180 sequences, while the test set contains 44 sequences. Table I provides a detailed comparison of the DSCA dataset and other DSA datasets. Notably, the DSCA dataset offers several distinct advantages, including a large number of samples, diverse image resolutions, and most importantly, public accessibility.

### III. PROPOSED METHOD

In this section, we introduce DSANet, a spatio-temporal network designed to segment CA in DSA sequences. The DSANet architecture comprises two encoding branches: the SEB and the TEB, along with a decoding branch, as depicted in Fig. 3. This network incorporates an additional TEB to extract temporal information from DSA sequences. After passing through the TEB, each sequential frame is treated as a token, and the TemporalFormer is developed to capture the global context and significant correlations among frames. In the bottleneck, an STF module is designed to fuse spatial and temporal features derived from different encoding branches.

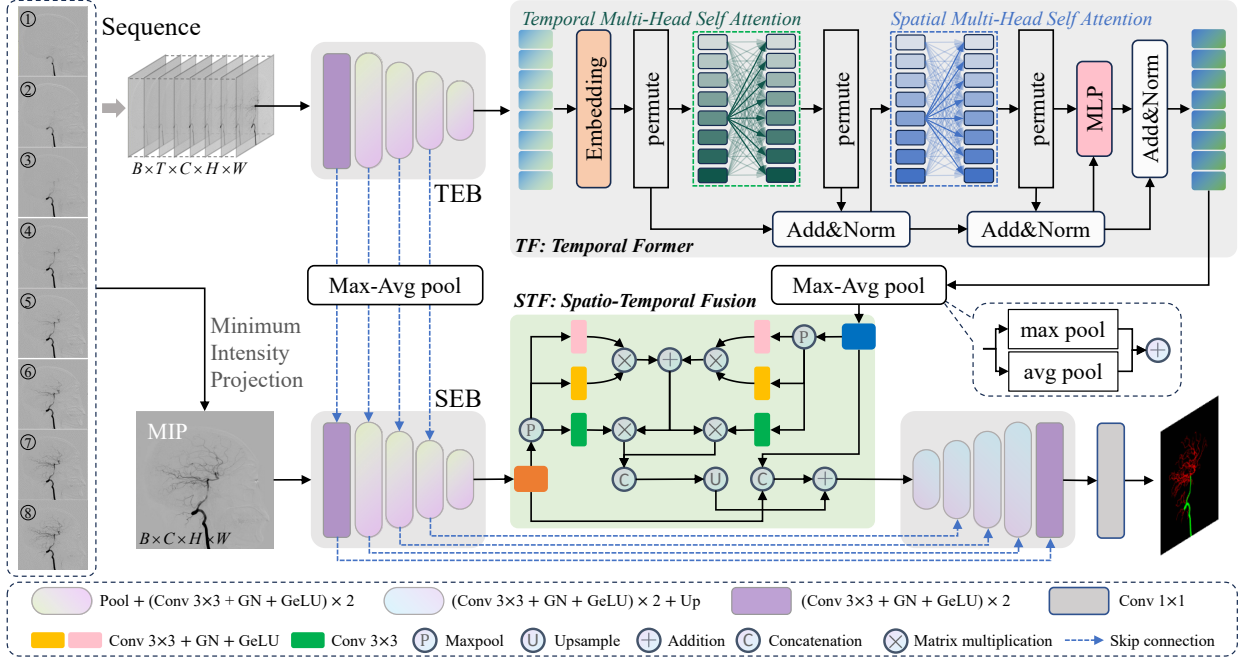


Fig. 3. Architecture of our proposed DSANet. It is primarily composed of two encoding branches, one decoding branch, and two modules: TemporalFormer (TF), Spatio-Temporal Fusion (STF).

### A. Encoding Branches

As shown in Fig. 3, there are two encoding branches: TEB at the top and SEB at the bottom. Although structurally similar, these branches function independently without weight sharing. Each encoding branch adopts a five-layer structure, comprising a single convolutional layer followed by four downsampling layers. The downsampling layer comprises a Maxpool block and a convolutional layer with double  $3 \times 3$  convolutional blocks, double GroupNorm blocks, and double Gelu blocks. The primary difference between the two encoding branches lies in their input.

1) *Spatial encoding branch*: In the SEB, the input is a 2D MIP image  $M \in \mathbb{R}^{B \times C \times H \times W}$ , where  $B$ ,  $C$ ,  $H$ , and  $W$  represent the batch size, number of channels, height, and width of  $M$ , respectively. This input setting is consistent with other 2D segmentation tasks in our subsequent comparisons.

2) *Temporal encoding branch*: In the TEB, the input is organized in 2D sequential frames denoted as  $S \in \mathbb{R}^{B \times T \times C \times H \times W}$ , where  $T$  represents the number of frames. The sequence encoding process is optimized for training convenience by merging  $B$  and  $T$  into  $N$ , where  $N = B \times T$ . Following the first convolutional layer, the value of  $C$  is doubled. Afterward, as the input sequence passes through the downsampling layer, both  $H$  and  $W$  are halved, and  $C$  is doubled. Each of the first four layers of the encoding branches includes an additional output serving as a skip connection. In the TEB, the skip connection needs to be downsampled in the  $T$  dimension and then concatenated with the skip connection in the SEB to form the final skip connection, and is subsequently fed into the corresponding layer in the decoder.

### B. TemporalFormer

The dynamic flows within DSA sequences possess rich temporal information, characterized by meaningful contextual correlations among frames. Consequently, this temporal information offers valuable assistance in segmenting cerebral arteries and categorizing them into BV and MTA. To effectively capture the global context and inter-frame correlations, we feed the features generated by each frame in the TEB into the TemporalFormer (TF), as depicted in Fig. 3.

We consider the features  $F_s \in \mathbb{R}^{N \times c \times h \times w}$  extracted from the TEB, where each frame feature is defined as  $f_s^t \in \mathbb{R}^{B \times c \times h \times w}$ . Here,  $c$ ,  $h$ , and  $w$  respectively represent the number of channels, the height, and the width of  $F_s$ . The index  $t \in \{0, T\}$  is treated as a token and inputted into the TF. Specifically,  $F_s$  is initially reshaped into  $\in \mathbb{R}^{B \times T \times c \times h \times w}$  to restore its original dimensions. Then, it is converted to a feature vector  $\mathcal{F}_s \in \mathbb{R}^{(Bhw) \times T \times c}$  by flattening  $B$ ,  $h$ , and  $w$ . Subsequently, we integrate learnable position encoding  $f_p \in \mathbb{R}^{T \times c}$  with  $\mathcal{F}_s$  by adding them together. Following this,  $\mathcal{F}_s$  is transformed into  $\in \mathbb{R}^{B \times (hwT) \times c}$  to generate a residual feature denoted as  $\mathcal{F}'_s$ , which is then restored. Afterwards,  $\mathcal{F}_s$  undergoes a temporal multi-head self-attention operation, which can be formulated as:

$$q_s, k_s, v_s = \mathbb{W}(\mathcal{F}_s), \quad (1)$$

$$\tilde{\mathcal{F}}_s = \text{Softmax}\left(\frac{q_s \times k_s^T}{\sqrt{d_k}}\right)v_s, \quad (2)$$

where  $q_s, k_s, v_s, \tilde{\mathcal{F}}_s \in \mathbb{R}^{(Bhw) \times T \times c}$  and  $d_k$  is the dimension of  $k_s$ , and  $\mathbb{W}$  represents a linear function. The output  $\tilde{\mathcal{F}}_s$  from the temporal self-attention block is reshaped to  $\in \mathbb{R}^{B \times (hwT) \times c}$ . This reshaped output is then added to  $\mathcal{F}'_s$  to obtain a new  $\tilde{\mathcal{F}}_s$  and  $\mathcal{F}'_s$ , where  $\tilde{\mathcal{F}}_s$  is equivalent to  $\mathcal{F}'_s$ . Next, we use a

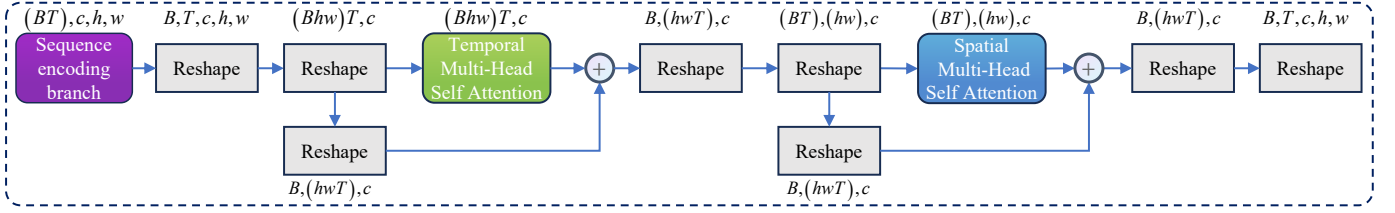


Fig. 4. The details of the dimension transformation process in TemporalFormer.

rearrange operation to map the new feature vector  $\tilde{\mathcal{F}}_s$  into  $\in \mathbb{R}^{(BT) \times (hw) \times c}$ . Similarly, a self-attention mechanism is applied in the spatial domain, as depicted in Equation (1) and (2). Given  $\tilde{\mathcal{F}}_s$  as the output of the spatial self-attention block, we reshape it into  $\mathbb{R}^{B \times (hwT) \times c}$  and add it to  $\tilde{\mathcal{F}}_s$  to get a new enhanced  $\hat{\mathcal{F}}_s$ . Following these self-attention blocks, an MLP block with two linear layers is applied to  $\hat{\mathcal{F}}_s$ . The details of the dimension transformation process are shown in Fig. 4. After passing through four TF layers, we finally obtain the enhanced feature  $\hat{\mathcal{F}}_s \in \mathbb{R}^{B \times (hwT) \times c}$ , and we restore it to  $\hat{F}_s \in \mathbb{R}^{B \times T \times c \times h \times w}$ . By downsampling  $\hat{F}_s$  in the  $T$  dimension, we get the new feature  $F_s \in \mathbb{R}^{B \times c \times h \times w}$ .

### C. Spatio-Temporal Fusion Module

To effectively fuse the spatial and temporal features from the encoder, we introduce an STF module. Given the feature  $F_m \in \mathbb{R}^{B \times c \times h \times w}$  from the SEB and the feature  $F_s \in \mathbb{R}^{B \times c \times h \times w}$  from the TF module, we initially apply Maxpool to both  $F_m$  and  $F_s$  to reduce the size of feature maps, yielding  $F'_m$  and  $F'_s \in \mathbb{R}^{B \times c \times \frac{h}{2} \times \frac{w}{2}}$ . Subsequently, the two features are passed through a shared convolutional block to generate feature vector  $Q_m, K_m, V_m, Q_s, K_s, V_s \in \mathbb{R}^{B \times c \times \frac{hw}{4}}$ . Afterwards,  $Q_m, Q_s$  are multiplied by  $K_m^T, K_s^T$ , respectively, and then dividing by  $\sqrt{c}$ . The weight matrices  $\alpha_i, \alpha_s \in \mathbb{R}^{B \times \frac{hw}{4}}$  are obtained through the softmax function, similar to Equation (2). The two weight matrices are then summed, and the result is respectively multiplied by  $V_m$  and  $V_s$  to get  $\tilde{F}'_m, \tilde{F}'_s \in \mathbb{R}^{B \times \frac{hw}{4}}$ , as depicted below:

$$\tilde{F}'_m = (\alpha_i + \alpha_s) \times V_m, \quad \tilde{F}'_s = (\alpha_i + \alpha_s) \times V_s. \quad (3)$$

We concatenate  $\tilde{F}'_m, \tilde{F}'_s$ , and use an upsample and reshape operation to map the result back to the standard feature map  $\tilde{F}'_{sm} \in \mathbb{R}^{B \times 2c \times h \times w}$ . Finally,  $F_m$  and  $F_s$  are concatenated and added with  $\tilde{F}'_{sm}$  in an element-wise manner to obtain the refined feature  $\hat{F}_{sm}$ , as defined by:

$$\hat{F}_{sm} = \tilde{F}'_{sm} + \text{Concat}(F_s, F_m), \quad (4)$$

where  $\text{Concat}$  indicates the concatenation operation. The feature  $\hat{F}_{sm}$  is then fed into the decoder for feature restoration.

### D. Loss Function

We utilize the cross-entropy loss ( $\mathcal{L}_{ce}$ ) and the dice loss ( $\mathcal{L}_{dice}$ ) to optimize the DSANet. The deep supervision mechanism [22] is also deployed to regularize the training process further. The  $\mathcal{L}_{ce}$  is defined by:

$$\mathcal{L}_{ce} = \frac{1}{N} \sum_j \mathcal{L}_j = -\frac{1}{N} \sum_j \sum_{k=1}^M y_{jk} \log(p_{jk}), \quad (5)$$

where  $N$  represents the total number of pixels,  $M$  gives the number of classes,  $y_{jk} \in \{0, 1\}$  defines whether pixel  $j$  belongs class  $k$  in the GT, and  $p_{jk} \in [0, 1]$  indicates the probability that pixel  $j$  belongs to class  $k$  in the predicted map. Similarly,  $\mathcal{L}_{dice}$  can be defined as:

$$\mathcal{L}_{dice} = 1 - \frac{2 \sum_{j=1}^N p_j \times y_j}{\sum_{j=1}^N p_j + \sum_{j=1}^N y_j}. \quad (6)$$

Therefore, the overall loss function is given by:

$$\mathcal{L}_{total} = \sum_{a=0}^2 \frac{1}{2^a} (\mathcal{L}_{ce}^a + \mathcal{L}_{dice}^a), \quad (7)$$

where  $a$  is the downsampling scale of the full-size output.

## IV. EXPERIMENTS

### A. Implementation Details

The proposed method was implemented with Python3.7, PyTorch 1.11.0, and Ubuntu 18.04. All training procedures were performed on RTX3090 (24G) GPUs. We used nnUNet as the backbone network. Stochastic Gradient Descent (SGD) was employed for model optimization during training, with a momentum of 0.99 and a weight decay of  $3e-5$ . The initial learning rate was set to 0.01 with a polynomial decay strategy. The maximum epoch number was set to 500 and one epoch contains 100 iterations for fair comparisons.

The preprocessing pipelines vary between training and testing. For training, we utilized a five-fold cross-validation method by dividing the 180 sequences in the training set, with four folds for training and one for validation. Each batch comprised 2 samples at  $512 \times 512$  pixels which were randomly cropped from images of varying dimensions. Additionally, common data augmentation methods were applied to optimize the training process, including random rotation, elastic deformation, random scaling, random cropping, gamma augmentation, and mirroring. For testing, we only perform mirroring operation for data augmentation. The testing procedure involved cropped patches of  $512 \times 512$  pixels from the test image via sliding windows. We applied padding with mirroring to ensure consistency in patch sizes. Subsequently, these patches were inputted into the network for prediction and then sequentially reconstructed to match the original image size. Finally, we compared the reconstructed predictions with the GT across the entire image. The performance metrics were determined based on the average values calculated by the five-fold cross-validation at the image level on the test set.

TABLE II

QUANTITATIVE COMPARISONS WITH DSA SEGMENTATION AND GENERAL SEGMENTATION METHODS ON DSCA FOR BV AND MTA. THE RESULTS ARE AVERAGE±STANDARD DEVIATION OBTAINED FROM THE FIVE-FOLD CROSS-VALIDATION. ALL METRICS ARE EXPRESSED AS PERCENTAGES (%).

Methods	JAC		Dice		SEN		PRE		AUC		
	BV	MTA	BV	MTA	BV	MTA	BV	MTA	BV	MTA	
DSA	Zhang <i>et al.</i> [26]	67.56±0.82	67.45±1.36	80.11±0.61	73.00±1.26	76.70±0.67	71.74±1.46	84.61±0.77	75.9±1.09	88.08±0.34	77.20±1.31
	MDCNN [7]	66.16±2.95	69.57±0.64	78.95±2.23	74.61±0.43	74.05±4.27	74.12±1.56	85.69±1.15	77.09±1.38	86.79±2.10	79.06±0.77
	ERNet [27]	73.39±0.67	78.01±1.07	84.19±0.46	82.61±1.18	81.67±1.56	80.75±1.50	87.49±1.01	87.80±2.02	90.60±0.76	86.03±1.54
General	UNet [8]	71.30±0.04	73.24±1.76	82.74±0.33	77.68±1.67	80.10±0.39	77.24±1.69	86.24±0.30	80.18±2.59	89.80±0.19	81.77±1.62
	CENet [33]	68.34±0.65	79.97±2.59	80.69±0.51	84.32±2.78	76.86±2.04	82.85±2.73	85.78±2.16	87.20±2.67	88.18±0.97	87.09±2.52
	CSNet [16]	73.02±0.93	81.28±1.87	83.95±0.65	85.37±1.79	80.77±2.05	84.11±2.07	87.98±1.23	89.13±1.63	90.17±0.99	88.85±2.24
	AttUNet [18]	69.88±0.78	74.58±1.00	81.73±0.57	79.10±0.92	76.51±1.59	77.85±1.26	88.47±1.12	82.68±1.01	88.07±0.77	82.31±1.13
	SwinUNet [20]	64.22±0.44	67.41±1.45	77.61±0.35	73.45±1.30	75.33±0.50	71.92±1.28	79.92±1.69	75.79±1.49	87.33±0.25	77.28±1.22
	MISSFormer [34]	70.09±0.37	78.97±3.67	81.89±0.21	84.06±3.37	79.10±0.62	82.41±3.39	85.58±0.91	86.87±3.54	89.30±0.30	87.08±3.19
	H2Former [35]	69.47±0.62	83.90±3.79	81.47±0.43	88.34±3.84	77.85±1.54	86.87±3.62	86.21±1.17	92.51±4.42	88.67±0.74	91.59±3.82
	TransUNet [19]	72.43±0.46	81.38±1.24	83.63±0.34	85.09±1.19	80.99±0.92	83.89±1.12	87.20±0.45	88.33±2.08	90.24±0.45	88.29±1.48
	nnUNet [22]	76.76±0.45	82.54±2.42	86.45±0.31	86.22±2.50	85.29±0.45	85.70±2.50	88.06±0.59	88.08±2.20	92.41±0.22	89.87±2.51
DSANet	<b>78.09±0.20</b>	<b>88.22±1.52</b>	<b>87.32±0.13</b>	<b>92.26±1.56</b>	<b>86.40±0.39</b>	<b>91.37±1.57</b>	<b>88.59±0.53</b>	<b>94.01±1.40</b>	<b>92.98±0.18</b>	<b>94.98±1.39</b>	

### B. Evaluation Metrics

To comprehensively evaluate the segmentation performance, the following metrics are calculated and compared: Jaccard (JAC) =  $TP / (TP + FP + FN)$ ; Dice =  $2 \times TP / (2 \times TP + FP + FN)$ ; Sensitivity (SEN) =  $TP / (TP + FN)$ ; Precision (PRE) =  $TP / (TP + FP)$ ; Area Under the ROC Curve (AUC), where TP, FP, TN, and FN are true positive, false positive, true negative, and false negative, respectively. The cIDice [36] is also used to evaluate vessel connectivity when measuring the entire CA.

### C. Cerebrovascular Segmentation Results

We extensively assessed our proposed method on the DSCA dataset, comparing it with state-of-the-art segmentation approaches, which include UNet [8], CENet [33], CSNet [16], AttentionUNet [17], SwinUNet [20], MISSFormer [34], H2Former [35], TransUNet [19], nnUNet [22], and [27]. Additionally, we also reproduced [26] and [7] for comparison, as their codes are not publicly available. The comparative results of segmentation are shown in Table II.

We can observe that DSANet achieves the best performance across all metrics for segmenting both MTA and BV, which indicates the superiority of our method. In MTA segmentation, DSANet holds a significant advantage over other methods in terms of JAC, Dice, SEN, and AUC, surpassing H2Former by 4.32%, 3.92%, 4.50%, and 3.39%, respectively. A statistical significance of ( $p < 0.05$ ) was obtained using a paired t-test between the two methods. In BV segmentation, the pixels of BV constitute a relatively small proportion of the total image pixels, which explains why our proposed method is not significantly ahead of the comparative method. Nevertheless, DSANet stands out as the only method higher than 78% in JAC and 86% in SEN, surpassing nnUNet by 1.33% and 1.11%, respectively. Similarly, it also outperforms nnUNet by 0.87% in Dice and 0.57% in AUC, highlighting its superior performance with statistical significance ( $p < 0.05$ ).

For a more intuitive comparison of CA segmentation performance across different methods, we also provide a visual comparison in Fig. 5. As we can see the shape and background of the CA are very intricate, with low contrast in small vessels.

In this challenging context, our DSANet effectively segments the CA, particularly ensuring small vessels with more robust connectivity, as indicated in the detailed orange boxes in ICA, ECA, and VA. In addition, skulls with deep contrast are mistakenly extracted as vessels in other methods, while our method successfully suppresses such false positives, as shown by the white arrows in ECA and VA in Fig. 5. In ICA, CENet and TransUNet perform well in segmenting vessels within the left orange box, while their performance diminishes in the right orange box. In contrast, DSANet achieves superior segmentation performance in both boxes. Furthermore, other methods erroneously segment the MTA in ECA (depicted in green), while DSANet effectively addresses this issue.

We also compare the performance of the entire CA without distinguishing BV and MTA to demonstrate the superiority of DSANet further. As indicated in Table III, DSANet holds a slight advantage over other methods in JAC, Dice, SEN, and AUC, surpassing the second-place method by 1.06%, 0.64%, 0.85%, and 0.43%, respectively, with statistical significance ( $p < 0.05$ ). To achieve precise segmentation, it is essential to focus on the intricate details of small vessel structures, which represent a minority of the total image pixels. Thus, cIDice [36] is employed to assess vessel connectivity. DSANet significantly outperforms other methods, surpassing nnUNet by 1.04% in cIDice with statistical significance ( $p < 0.001$ ).

### D. Ablation Study

We performed extensive ablation experiments on the DSCA dataset to illustrate the effectiveness of the components in DSANet. Utilizing nnUNet as the baseline, we systematically evaluated the influence of each component on the segmentation results, as shown in Table IV.

1) *Ablation for temporal encoding branch:* In this section, we present a comparative analysis of metrics including JAC, Dice, SEN, PRE, and AUC to assess the impact of integrating TEB. We incorporate TEB with nnUNet while maintaining consistent experimental settings. The ablation results, presented in the 4th row of Table IV, demonstrate a significant improvement in both BV and MTA segmentation.

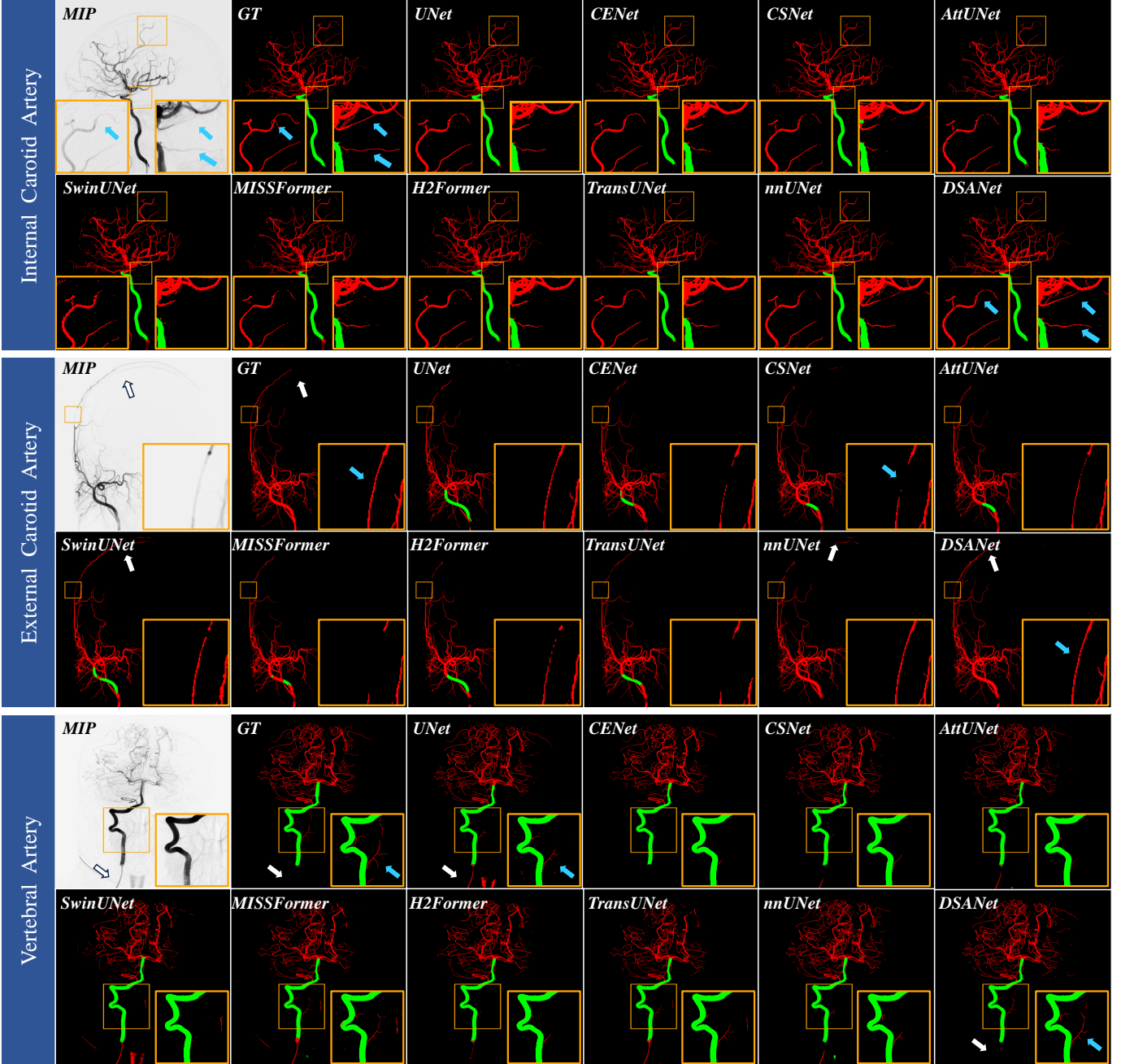


Fig. 5. Segmentation results on the DSCA dataset. Green is MTA, and red is BV. Enlarged viewing for better clarity.

This is primarily attributed to the integration of dynamic flow information. Notably, the incorporation of TEB resulted in an increase of over 1% in JAC, Dice, SEN, PRE, and AUC in MTA.

2) *Ablation for TemporalFormer*: Subsequently, we validate the impact of TF based on the established foundation of the TEB. As depicted in the fifth row of Table IV, all experimental outcomes have shown improvement to varying degrees compared to the fourth row. The enhancement in the segmentation results for MTA is more prominent than that for BV. Specifically, the SEN indicator has reached its optimal level in MTA in this method, reaching 91.86%.

3) *Ablation for spatio-temporal fusion module*: Similarly, we assess the superiority of the STF module in conjunction with the TEB. Comparing the results in the sixth and fourth rows of Table IV, it is obvious that incorporating the STF module promotes better segmentation performance. Among them, the SEN and AUC metrics reach their optimal BV segmentation for our method, increasing the TEB by 0.72% and 0.35%, respectively. In the PRE metric, it slightly drops by 0.28% and 0.21% in BV, while outperforming them by 4.95% and 2.00% in MTA, compared to the baseline and the TEB, respectively. The last row in Table IV outlines our results. A comprehensive review of the ablation experiments in the table explicitly illustrates the effectiveness of our method and its

TABLE III

QUANTITATIVE COMPARISONS WITH DSA SEGMENTATION AND GENERAL SEGMENTATION METHODS ON DSCA FOR THE ENTIRE VESSEL. THE RESULTS ARE AVERAGE $\pm$ STANDARD DEVIATION OBTAINED FROM FIVE-FOLD CROSS-VALIDATION. ALL METRICS ARE BASED ON PERCENTAGES (%).

Methods		clDice	JAC	Dice	SEN	PRE	AUC
DSA	Zhang <i>et al.</i> [26]	81.87 $\pm$ 0.85	76.63 $\pm$ 0.66	86.49 $\pm$ 0.44	83.71 $\pm$ 0.54	89.92 $\pm$ 0.61	91.62 $\pm$ 0.27
	MDCNN [7]	80.00 $\pm$ 2.85	75.19 $\pm$ 2.17	85.50 $\pm$ 1.44	81.58 $\pm$ 3.12	90.61 $\pm$ 0.99	90.58 $\pm$ 1.53
	ERNet [27]	85.36 $\pm$ 0.39	79.65 $\pm$ 0.36	88.40 $\pm$ 0.23	85.75 $\pm$ 1.15	91.66 $\pm$ 0.90	92.68 $\pm$ 0.55
General	UNet [8]	84.34 $\pm$ 0.29	78.41 $\pm$ 0.35	87.61 $\pm$ 0.23	85.47 $\pm$ 0.36	90.27 $\pm$ 0.22	92.51 $\pm$ 0.18
	CENet [33]	81.01 $\pm$ 0.40	75.06 $\pm$ 0.44	85.45 $\pm$ 0.31	81.79 $\pm$ 1.70	90.04 $\pm$ 1.68	90.66 $\pm$ 0.80
	CSNet [16]	84.84 $\pm$ 0.82	79.06 $\pm$ 0.71	88.07 $\pm$ 0.45	84.97 $\pm$ 1.63	91.71 $\pm$ 0.11	92.29 $\pm$ 0.79
	AttUNet [18]	82.63 $\pm$ 0.52	76.77 $\pm$ 0.46	86.56 $\pm$ 0.29	82.10 $\pm$ 1.12	<b>92.09 <math>\pm</math> 0.88</b>	90.86 $\pm$ 0.54
	SwinUNet [20]	77.65 $\pm$ 0.33	72.68 $\pm$ 0.42	81.58 $\pm$ 0.22	73.24 $\pm$ 0.27	86.99 $\pm$ 0.28	90.48 $\pm$ 0.14
	MISSFormer [34]	82.78 $\pm$ 0.39	77.01 $\pm$ 0.21	86.78 $\pm$ 0.13	83.92 $\pm$ 0.55	90.17 $\pm$ 0.66	91.73 $\pm$ 0.26
	H2Former [35]	82.30 $\pm$ 0.69	76.10 $\pm$ 0.42	86.15 $\pm$ 0.28	82.59 $\pm$ 1.09	90.56 $\pm$ 0.85	91.07 $\pm$ 0.52
	TransUnet [19]	84.68 $\pm$ 0.40	78.44 $\pm$ 0.31	87.71 $\pm$ 0.20	85.23 $\pm$ 0.80	90.70 $\pm$ 0.57	92.38 $\pm$ 0.38
	nnUNet [22]	87.54 $\pm$ 0.25	81.70 $\pm$ 0.23	89.69 $\pm$ 0.14	88.45 $\pm$ 0.28	91.17 $\pm$ 0.17	94.01 $\pm$ 0.14
DSANet		<b>88.58 <math>\pm</math> 0.13</b>	<b>82.76 <math>\pm</math> 0.16</b>	<b>90.33 <math>\pm</math> 0.09</b>	<b>89.30 <math>\pm</math> 0.23</b>	91.56 $\pm$ 0.32	<b>94.44 <math>\pm</math> 0.11</b>

TABLE IV

ABLATION STUDY OF THESE COMPONENTS OF THE PROPOSED DSANet. THE RESULTS ARE AVERAGE $\pm$ STANDARD DEVIATION OBTAINED FROM THE FIVE-FOLD CROSS-VALIDATION EXPERIMENT. ALL METRICS ARE EXPRESSED AS PERCENTAGES (%).

Ablation Sets			JAC		Dice		SEN		PRE		AUC	
TEB	TF	STF	BV	MTA								
			76.76 $\pm$ 0.45	82.54 $\pm$ 2.42	86.45 $\pm$ 0.31	86.22 $\pm$ 2.50	85.29 $\pm$ 0.45	85.70 $\pm$ 2.50	88.06 $\pm$ 0.59	88.08 $\pm$ 2.20	92.41 $\pm$ 0.22	89.87 $\pm$ 2.51
✓			77.40 $\pm$ 0.26	84.02 $\pm$ 4.82	86.87 $\pm$ 0.18	88.25 $\pm$ 4.87	86.12 $\pm$ 0.44	87.20 $\pm$ 5.12	87.99 $\pm$ 0.67	91.03 $\pm$ 3.75	92.83 $\pm$ 0.21	91.30 $\pm$ 4.67
✓	✓		78.02 $\pm$ 0.22	86.00 $\pm$ 1.43	87.25 $\pm$ 1.43	89.91 $\pm$ 1.52	86.56 $\pm$ 0.10	<b>91.86<math>\pm</math>1.05</b>	88.30 $\pm$ 0.22	92.81 $\pm$ 1.32	93.05 $\pm$ 0.05	93.18 $\pm$ 1.19
✓		✓	77.83 $\pm$ 0.33	86.14 $\pm$ 2.21	87.14 $\pm$ 0.21	89.99 $\pm$ 2.29	<b>86.84<math>\pm</math>0.60</b>	88.99 $\pm$ 2.18	87.78 $\pm$ 0.66	93.03 $\pm$ 2.63	<b>93.18<math>\pm</math>0.29</b>	93.34 $\pm$ 2.00
✓	✓	✓	<b>78.09<math>\pm</math>0.20</b>	<b>88.22<math>\pm</math>1.52</b>	<b>87.32<math>\pm</math>0.13</b>	<b>92.26<math>\pm</math>1.56</b>	86.40 $\pm$ 0.39	91.37 $\pm$ 1.57	<b>88.59<math>\pm</math>0.53</b>	<b>94.01<math>\pm</math>1.40</b>	92.98 $\pm$ 0.18	<b>94.98<math>\pm</math>1.39</b>

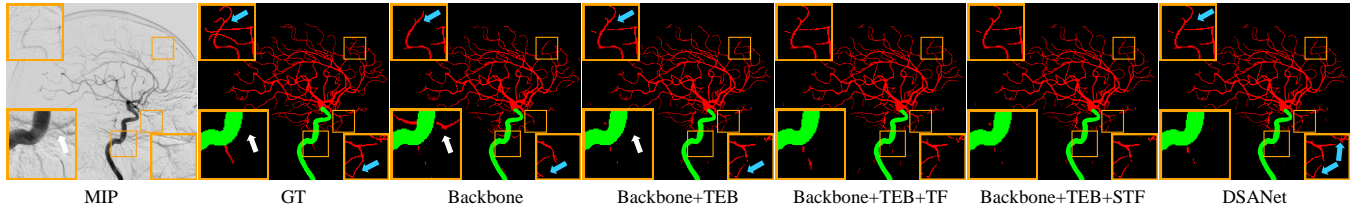


Fig. 6. The ablation study results for baseline, DSANet, and the components of DSANet, with zoomed views for better visualization.

components.

In addition, we also provide visual comparisons in Fig. 6. The white arrows in the figure highlight a pseudo-shadow resembling a residual skull. While nnUNet misclassifies it as a vessel, our method successfully avoids such misclassification after the integration of TEB. Moreover, the small terminal vessels are better preserved in comparison with the baseline, as indicated by the blue arrows in the fourth column of Fig. 6. Additionally, through the integration of TF and STF in DSANet, the connectivity of small vessels shows obvious improvements, as depicted in the zoomed orange box and blue arrows of the last column of Fig. 6.

## V. DISCUSSION

### A. DSCA: Promoting Clinical Cerebrovascular Analysis

The DSCA dataset comprises 224 sequences, each meticulously annotated pixel by pixel using MIP images. It includes ICA, ECA, and VA, with further subclassification of ICA and VA into BV and MTA. This classification closely aligns

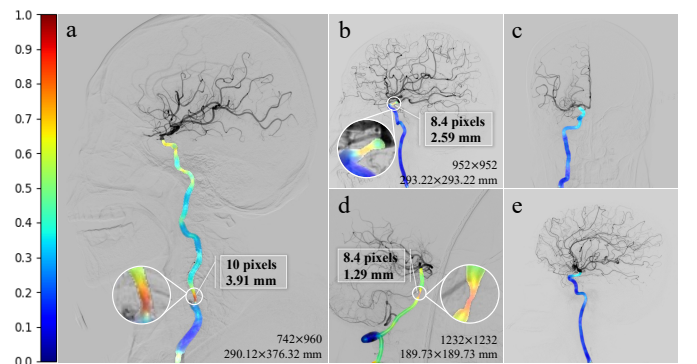


Fig. 7. Several instances where the MTA class is employed to assess stenosis. The more intense the red color, the more severe the stenosis.

with the requirements of clinical analysis. Previous studies have demonstrated the value of precisely measuring carotid stenosis [37]. The extraction of MTA facilitates automated diameter calculations for ICA and VA, particularly in evaluating

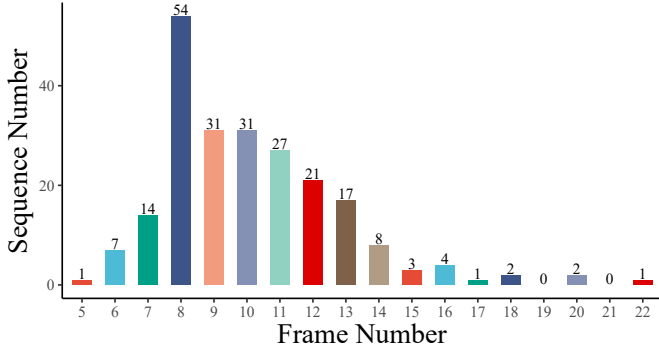


Fig. 8. The distribution of the number of frames in DSCA.

biomarkers at stenosis sites. Fig. 7 reveals several instances where MTA is used to assess stenosis in the main trunk of the artery. In Fig. 7-(a), (b), (d), the diameter of the stenosis region can be easily determined from the segmented MTA. Moreover, the color representation of the arterial main trunk appears normal in the absence of stenosis, as illustrated in Fig. 7-(c), (e). Similarly, vascular density can be obtained for individually extracted BV to support clinical applications effectively, as demonstrated in the previous research for evaluating thrombolysis scores in ischemic stroke [29].

### B. Why Resample 8 Frames for Training?

To meet the input specifications of the model, we resampled the unfixed-length sequential frames to a fixed length. This procedure is necessary based on the observation that the majority of frames cluster around 8 frames, as illustrated in Fig. 8. Resampling inputs that exceed 8 frames could introduce excessive resampling error, which in turn compromises the segmentation performance of the model. Conversely, resampling fewer than 8 frames results in a significant loss of temporal information in the DSA sequence, impeding the model’s ability to capture sufficient dynamic flow features and similarly degrading segmentation performance. The experimental results, illustrated in Fig. 9, confirm the finding that optimal segmentation performance is achieved when the input is resampled to 8 frames. Deviations from this resampling size, whether higher or lower, are associated with a decline in the model’s segmentation efficacy. Consequently, we affirm that resampling consecutive frames to a length of 8 frames provides a comparatively optimal strategy.

### C. DSANet: Effectively Handle Complex Situations

It is challenging to accurately segment CA due to small vessels with low visibility and ambiguity between vessels and residual skull structures. To further validate the effectiveness of our approach, we generate heatmaps for the final layer output of the decoder and make comparisons with state-of-the-art methods, as shown in Fig. 10. In the 2nd and 4th rows, all methods exhibit a positive response in MTA. Additionally, a comparison of the 1st and 3rd rows reveals that our DSANet produces a stronger response than UNet, TransUNet, and

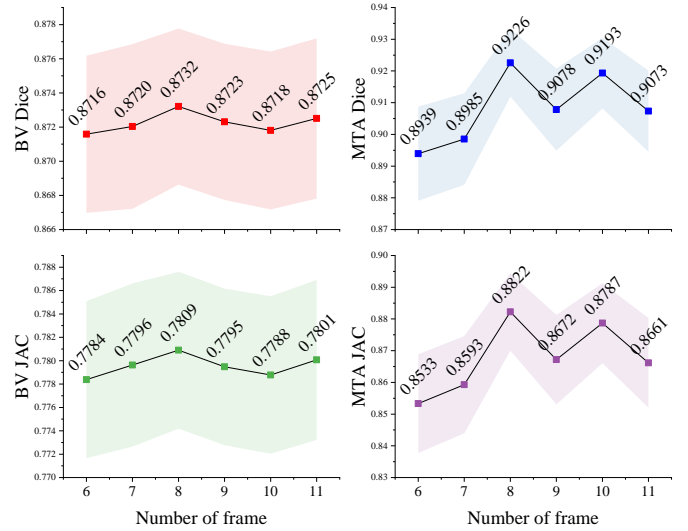


Fig. 9. The influence of frame numbers on experiments. The evaluation metrics include Dice and JAC.

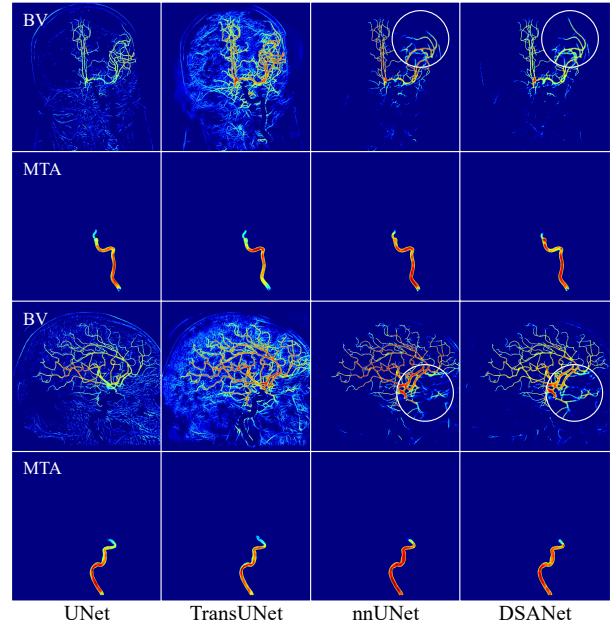


Fig. 10. Heatmaps of the final layer output for different methods.

nnUNet on small vascular structures in BV, particularly in the areas highlighted by the white circles. Meanwhile, UNet and TransUNet are more susceptible to background artifacts and noise than the proposed DSANet, as shown in the 1st and 2nd columns of BV. This highlights the superior performance of our method in suppressing background interferences.

## VI. CONCLUSION AND FUTURE WORKS

In this paper, we have established the DSCA dataset, a large, carefully designed, and systematically annotated dataset for CA segmentation in DSA sequences. To our knowledge, the DSCA is the first publicly available DSA sequence dataset. It not only has pixel-wise vessel annotations but also includes subdivisions for BV and MTA, which are closely related to the

clinical treatment of CVDs. This dataset will be highly beneficial for researchers in CVD studies. Furthermore, we have proposed DSANet, a spatio-temporal network for CA segmentation. Unlike 2D segmentation methods, DSANet incorporates an independent temporal encoding branch to capture dynamic temporal information. It integrates TemporalFormer and Spatio-Temporal Fusion modules to further process spatio-temporal features. Extensive experiments demonstrate the effectiveness of our method, particularly small vessels, holding significant potential for clinical applications.

## REFERENCES

- [1] G. A. Roth, G. A. Mensah, C. O. Johnson, et al. Global burden of cardiovascular diseases and risk factors, 1990–2019: update from the gbd 2019 study. *Journal of the American College of Cardiology*, 76(25):2982–3021, 2020.
- [2] M. Goni, N. Ruhaiyem, M. Mustapha, A. Achuthan, and C. Nassir. Brain vessel segmentation using deep learning—a review. *IEEE Access*, 2022.
- [3] C. P. Hess. Imaging in Cerebrovascular Disease. In *Molecular, Genetic, and Cellular Advances in Cerebrovascular Diseases*, pages 1–23. World Scientific, 2018.
- [4] P. Zou, P. Chan, and P. Rockett. A model-based consecutive scanline tracking method for extracting vascular networks from 2-d digital subtraction angiograms. *IEEE Transactions on Medical Imaging*, 28(2):241–249, 2008.
- [5] N. Sang, H. Li, W. Peng, and T. Zhang. Knowledge-based adaptive thresholding segmentation of digital subtraction angiography images. *Image and Vision Computing*, 25(8):1263–1270, 2007.
- [6] Z.n Chen, L. Xie, Y. Chen, Q. Zeng, Q.n ZhuGe, J. Shen, C. Wen, and Y. Feng. Generative adversarial network based cerebrovascular segmentation for time-of-flight magnetic resonance angiography image. *Neurocomputing*, 488:657–668, 2022.
- [7] C. Meng, K. Sun, S. Guan, Q. Wang, R. Zong, and L. Liu. Multiscale dense convolutional neural network for dsa cerebrovascular segmentation. *Neurocomputing*, 373:123–134, 2020.
- [8] O. Ronneberger, P. Fischer, and T. Brox. U-net: Convolutional networks for biomedical image segmentation. In *Medical Image Computing and Computer-Assisted Intervention—MICCAI 2015: 18th International Conference, Munich, Germany, October 5-9, 2015, Proceedings, Part III 18*, pages 234–241. Springer, 2015.
- [9] H. Fu, Y. Xu, S. Lin, D. Kee Wong, and J. Liu. Deepvessel: Retinal vessel segmentation via deep learning and conditional random field. In *Medical Image Computing and Computer-Assisted Intervention—MICCAI 2016: 19th International Conference, Athens, Greece, October 17-21, 2016, Proceedings, Part II 19*, pages 132–139. Springer, 2016.
- [10] P. Liskowski and K. Krawiec. Segmenting retinal blood vessels with deep neural networks. *IEEE Transactions on Medical Imaging*, 35(11):2369–2380, 2016.
- [11] Y. Ma, H. Hao, J. Xie, H. Fu, J. Zhang, J. Yang, Z. Wang, J. Liu, Y. Zheng, and Y. Zhao. ROSE: a retinal oct-angiography vessel segmentation dataset and new model. *IEEE Transactions on Medical Imaging*, 40(3):928–939, 2020.
- [12] W. Liu, H. Yang, T. Tian, Z. Cao, X. Pan, W. Xu, Y. Jin, and F. Gao. Full-resolution network and dual-threshold iteration for retinal vessel and coronary angiograph segmentation. *IEEE Journal of Biomedical and Health Informatics*, 26(9):4623–4634, 2022.
- [13] H. Wang, P. Cao, J. Wang, and O. Zaiane. Uctransnet: rethinking the skip connections in u-net from a channel-wise perspective with transformer. In *Proceedings of the AAAI Conference on Artificial Intelligence*, volume 36, pages 2441–2449, 2022.
- [14] L. Mou, L. Chen, J. Cheng, Z. Gu, Y. Zhao, and J. Liu. Dense dilated network with probability regularized walk for vessel detection. *IEEE Transactions on Medical Imaging*, 39(5):1392–1403, 2019.
- [15] Y. Ye, C. Pan, Y. Wu, S. Wang, and Y. Xia. MFI-Net: Multiscale feature interaction network for retinal vessel segmentation. *IEEE Journal of Biomedical and Health Informatics*, 26(9):4551–4562, 2022.
- [16] L. Mou, Y. Zhao, H. Fu, Y. Liu, J. Cheng, Y. Zheng, P. Su, J. Yang, L. Chen, A. F. Frangi, et al. CS2-Net: Deep learning segmentation of curvilinear structures in medical imaging. *Medical Image Analysis*, 67:101874, 2021.
- [17] J. Schlemper, O. Oktay, M. Schaap, M. Heinrich, B. Kainz, B. Glocker, and D. Rueckert. Attention gated networks: Learning to leverage salient regions in medical images. *Medical Image Analysis*, 53:197–207, 2019.
- [18] S. Zhang, H. Fu, Y. Yan, Y. Zhang, Q. Wu, M. Yang, M. Tan, and Y. Xu. Attention guided network for retinal image segmentation. In *Medical Image Computing and Computer Assisted Intervention—MICCAI 2019: 22nd International Conference, Shenzhen, China, October 13–17, 2019, Proceedings, Part I 22*, pages 797–805. Springer, 2019.
- [19] J. Chen, Y. Lu, Q. Yu, X. Luo, E. Adeli, Y. Wang, L. Lu, A. Yuille, and Y. Zhou. Transunet: Transformers make strong encoders for medical image segmentation. *arXiv preprint arXiv:2102.04306*, 2021.
- [20] H. Cao, Y. Wang, J. Chen, D. Jiang, X. Zhang, Q. Tian, and M. Wang. Swin-unet: Unet-like pure transformer for medical image segmentation. In *European Conference on Computer Vision*, pages 205–218. Springer, 2022.
- [21] A. Hatamizadeh, Y. Tang, V. Nath, D. Yang, A. Myronenko, B. Landman, H. Roth, and D. Xu. Unetr: Transformers for 3D medical image segmentation. In *Proceedings of the IEEE/CVF Winter Conference on Applications of Computer Vision*, pages 574–584, 2022.
- [22] F. Isensee, P. Jaeger, S. Kohl, J. Petersen, and K. Maier-Hein. nnU-Net: a self-configuring method for deep learning-based biomedical image segmentation. *Nature Methods*, 18(2):203–211, 2021.
- [23] Y. Zhang, Y. Gao, G. Zhou, J. He, J. Xia, G. Peng, X. Lou, S. Zhou, H. Tang, and Y. Chen. Centerline-supervision multi-task learning network for coronary angiography segmentation. *Biomedical Signal Processing and Control*, 82:104510, 2023.
- [24] S. Fan, Y. Bian, H. Chen, Y. Kang, Q. Yang, and T. Tan. Unsupervised cerebrovascular segmentation of tof-mra images based on deep neural network and hidden markov random field model. *Frontiers in Neuroinformatics*, 13:77, 2020.
- [25] L. Xie, Z. Chen, X. Sheng, Q. Zeng, J. Huang, C. Wen, L. Wen, G. Xie, and Y. Feng. Semi-supervised region-connectivity-based cerebrovascular segmentation for time-of-flight magnetic resonance angiography image. *Computers in Biology and Medicine*, 149:105972, 2022.
- [26] M. Zhang, Ch. Zhang, X. Wu, X. Cao, G. Young, H. Chen, and X. Xu. A neural network approach to segment brain blood vessels in digital subtraction angiography. *Computer Methods and Programs in Biomedicine*, 185:105159, 2020.
- [27] W. Xu, H. Yang, Y. Shi, T. Tan, W. Liu, X. Pan, Y. Deng, F. Gao, and R. Su. Ernet: Edge regularization network for cerebral vessel segmentation in digital subtraction angiography images. *IEEE Journal of Biomedical and Health Informatics*, 2023.
- [28] A. Vepa, A. Choi, N. Nakhaci, et al. Weakly-supervised convolutional neural networks for vessel segmentation in cerebral angiography. In *Proceedings of the IEEE/CVF Winter Conference on Applications of Computer Vision*, pages 585–594, 2022.
- [29] R. Su, S. Cornelissen, M. Van Der Sluijs, et al. autoTICI: Automatic brain tissue reperfusion scoring on 2D DSA images of acute ischemic stroke patients. *IEEE Transactions on Medical Imaging*, 40(9):2380–2391, 2021.
- [30] Y. Fu, J. Fang, B. Quachtran, N. Chachkhiani, and F. Scalzo. Vessel detection on cerebral angiograms using convolutional neural networks. In *Advances in Visual Computing: 12th International Symposium, ISVC 2016, Las Vegas, NV, USA, December 12-14, 2016, Proceedings, Part I 12*, pages 659–668. Springer, 2016.
- [31] S. Klein, M. Staring, K. Murphy, M. Viergever, and J. Pluim. Elastix: a toolbox for intensity-based medical image registration. *IEEE Transactions on Medical Imaging*, 29(1):196–205, 2009.
- [32] P. Yushkevich, Y. Gao, and G. Gerig. ITK-SNAP: An interactive tool for semi-automatic segmentation of multi-modality biomedical images. In *2016 38th Annual International Conference of the IEEE Engineering in Medicine and Biology Society (EMBC)*, pages 3342–3345. IEEE, 2016.
- [33] Z. Gu, J. Cheng, H. Fu, K. Zhou, H. Hao, Y. Zhao, T. Zhang, S. Gao, and J. Liu. Ce-net: Context encoder network for 2d medical image segmentation. *IEEE Transactions on Medical Imaging*, 38(10):2281–2292, 2019.
- [34] X. Huang, Z. Deng, D. Li, X. Yuan, and Y. Fu. MISSFormer: an effective transformer for 2D medical image segmentation. *IEEE Transactions on Medical Imaging*, 2022.
- [35] A. He, K. Wang, T. Li, C. Du, S. Xia, and H. Fu. H2Former: An efficient hierarchical hybrid transformer for medical image segmentation. *IEEE Transactions on Medical Imaging*, 2023.
- [36] S. Shit, J. Paetzold, A. Sekuboyina, I. Ezhov, A. Unger, A. Zhylyka, J. Pluim, U. Bauer, and B. Menze. clDice—a novel topology-preserving loss function for tubular structure segmentation. In *Proceedings of the IEEE/CVF Conference on Computer Vision and Pattern Recognition*, pages 16560–16569, 2021.
- [37] P. Rothwell, R. Gibson, J. Slattery, and C. Warlow. Prognostic value and reproducibility of measurements of carotid stenosis. a comparison

of three methods on 1001 angiograms. european carotid surgery trialists' collaborative group. *Stroke*, 25(12):2440-2444, 1994.